



Cite this: *Nanoscale Adv.*, 2022, 4, 3083

# Structural modification of salt-promoted MgO sorbents for intermediate temperature CO<sub>2</sub> capture†

Dasol Choi <sup>a</sup> and Youngjune Park <sup>\*ab</sup>

MgO-based sorbents are a promising option for CO<sub>2</sub> capture at intermediate temperatures. MgO-based sorbents are often hybridized with alkali metal salts to promote the CO<sub>2</sub> capture performance. However, MgO-based sorbents often suffer a rapid decrement of CO<sub>2</sub> capture performance during multicycle carbonation–calcination reactions due to the reduction of active sites. In this study, we attempted to enhance the durability of MgO-based sorbents by modifying their morphology. A tubular-shaped MgO-based sorbent was synthesized using a carbon nanotube template. Various characterization experiments and evaluations were performed with the synthesized MgO-based materials. The MgO sample with modified structure exhibited a specific morphology consisting of elongated plate-like structures separated by empty spaces. This separation is expected to prevent MgO agglomeration and preserve the modified morphology during iterative CO<sub>2</sub> capture reactions. The MgO with modified structure achieved higher cycling stability with four times slower performance decay than the control MgO, even though identical chemical compositions were applied.

Received 5th April 2022  
Accepted 9th June 2022

DOI: 10.1039/d2na00213b

rsc.li/nanoscale-advances

## Introduction

In response to the steeply rising demand for CO<sub>2</sub> reduction, CO<sub>2</sub> capture, utilization, and storage (CCUS) techniques are being intensively studied for various CO<sub>2</sub> emission conditions.<sup>1,2</sup> In particular, CO<sub>2</sub> emissions at intermediate temperatures (*i.e.*, 200–400 °C) are important CCUS targets that include post-combustion flue gas, CO<sub>2</sub>/H<sub>2</sub> separation after the water–gas shift reaction, and the steam reforming reaction of methanol.<sup>3–5</sup> Chemical adsorption of CO<sub>2</sub> on solid MgO is considered a suitable option for CO<sub>2</sub> capture at intermediate temperatures, which is based on the reversible carbonation–calcination reaction of MgO–MgCO<sub>3</sub> (*i.e.*, MgO (s) + CO<sub>2</sub> (g) ⇌ MgCO<sub>3</sub> (s)) at working temperatures of 250–400 °C.<sup>6–8</sup> Solid MgO directly captures CO<sub>2</sub> from gas streams to form MgCO<sub>3</sub>, and the regeneration can be easily performed by heating the MgCO<sub>3</sub> beyond 400 °C to produce MgO and a CO<sub>2</sub>-enriched stream.<sup>8</sup> This process has the distinct advantage of high theoretical CO<sub>2</sub> capture capacity (24.8 mol CO<sub>2</sub> per kg MgO). Furthermore, the

energy requirement for regeneration can be moderated by heat recovery from the exothermic CO<sub>2</sub> capture step at 350 °C.<sup>9</sup>

To apply MgO-based sorbents to the CO<sub>2</sub> capture process, further enhancements of CO<sub>2</sub> capture performance and durability must be achieved. The gas–solid reaction between MgO and CO<sub>2</sub> often suffers from the low conversion of MgO to MgCO<sub>3</sub> due to the stable lattice structure of Mg<sup>2+</sup>–O<sup>2-</sup> and the passivation of unreacted inner MgO by MgCO<sub>3</sub> on the surface at the initial stage of carbonation.<sup>7,10</sup> Salt-promoted MgO carbonation has been intensively studied by applying mixtures of various alkali nitrate salts and alkali carbonate salts, which can significantly enhance the overall MgO carbonation efficiency.<sup>11–15</sup> For example, it was reported that the salt mixture 2(Li<sub>0.44</sub>K<sub>0.56</sub>)NO<sub>3</sub>/(Na<sub>0.5</sub>K<sub>0.5</sub>)<sub>2</sub>CO<sub>3</sub> exhibits highly improved CO<sub>2</sub> capture performance.<sup>16,17</sup>

Enhancing the durability of MgO-based sorbents is another challenge. Even though high performance MgO-based sorbents can be achieved by salt-promotion, a rapid decrement of recyclability is often observed during multicycle carbonation–calcination reactions due to the reduction of active sites by agglomeration of MgO particles.<sup>13,15,16,18–20</sup> Sintering of MgCO<sub>3</sub> is considered a principal factor that provokes agglomeration, which is caused by the low Tammann temperature of MgCO<sub>3</sub> and accelerated atomic diffusion at the interface between MgCO<sub>3</sub> and the molten salt promoter.<sup>16,18,21</sup> In addition, the chemisorption of CO<sub>2</sub> can cause the expansion of MgO particle volume due to the density difference between MgO and MgCO<sub>3</sub>. Therefore, it is thought that the volume expansion of particles

<sup>a</sup>School of Earth Sciences and Environmental Engineering, Gwangju Institute of Science and Technology (GIST), 123 Cheomdangwagi-ro, Buk-gu, Gwangju 61005, Republic of Korea. E-mail: young@gist.ac.kr

<sup>b</sup>Research Center for Innovative Energy and Carbon Optimized Synthesis for Chemicals (Inn-ECOSysChem), Gwangju Institute of Science and Technology (GIST), 123 Cheomdangwagi-ro, Buk-gu, Gwangju 61005, Republic of Korea

† Electronic supplementary information (ESI) available. See <https://doi.org/10.1039/d2na00213b>



accelerates agglomeration and blocks small pores, resulting in a reduction of active sites available for the reversible reaction.

This study aims to enhance the durability of MgO-based sorbents in the reversible carbonation–calcination reaction by modifying the morphology to preserve active sites. For this, tubular-shaped MgO particles were synthesized to restrain grain overlapping by producing inner empty spaces. In order to produce tubular MgO particles, multi-walled carbon nanotubes (CNT) were used as a template for the precipitated MgCO<sub>3</sub>. Two samples were prepared, one by removing and one by retaining the CNT template, and their reaction behaviors were compared. The prepared MgO sorbents were characterized *via* Raman, XRD, TGA, and BET analyses, and morphology evolution during the multicycle reaction was observed by SEM and TEM. The relationship between controlled morphology and multicycle CO<sub>2</sub> capture performance was discussed.

## Experimental

### Materials

Magnesium chloride (MgCl<sub>2</sub>, 98%), multi-walled carbon nanotubes (CNT, >90% carbon basis, *D* = 110–170 nm, *L* = 5–9 μm), lithium nitrate (LiNO<sub>3</sub>, 99%), potassium nitrate (KNO<sub>3</sub>, 99%), sodium carbonate (Na<sub>2</sub>CO<sub>3</sub>, 99%), potassium carbonate (K<sub>2</sub>CO<sub>3</sub>, 99%), hydrochloric acid (HCl, 99%), and nitric acid (HNO<sub>3</sub>, 99%) were purchased from Sigma-Aldrich Co. (USA). N<sub>2</sub> gas and CO<sub>2</sub> gas were supplied by Shinil Gas Co., Ltd (Republic of Korea).

### Preparation of MgO/CNT sorbents

The synthesis method of MgO precipitated on the CNT template was modified by referring to the literature.<sup>22,23</sup> As the alkali metal salt (AMS) promoter, a hybrid salt of nitrate and carbonate, 2(Li<sub>0.44</sub>K<sub>0.56</sub>)NO<sub>3</sub>/(Na<sub>0.5</sub>K<sub>0.5</sub>)<sub>2</sub>CO<sub>3</sub>, was employed for carbonation enhancement.<sup>16,17</sup> Three types of MgO-based sorbents, MgO/CNT<sub>N<sub>2</sub></sub>, MgO/CNT<sub>Air</sub>, and MgO, were synthesized. MgO/CNT<sub>N<sub>2</sub></sub> was a MgO-based sorbent on a CNT template. MgO/CNT<sub>Air</sub> was a MgO-based sorbent on a sacrificial CNT template that was thermally removed afterward. The control sample MgO was prepared without CNT but in the same manner. The samples are listed in Table 1. The ratio of AMS promoter to MgO was determined according to the referenced studies.<sup>16,17</sup>

**CNT activation.** In order to purify and activate CNT, reagent CNT was treated with strong acid. 100 mL of 5 M HNO<sub>3</sub> and 5 M HCl solution was prepared by mixing 36 mL of HCl, 22 mL of HNO<sub>3</sub>, and 42 mL of deionized water. Then 0.500 g of CNT was

added to the acid solution. The CNT-added solution was sonicated for 30 min, stirred with a magnetic bar at 300 rpm for 2 h, and aged for 24 h at room temperature. Treated CNT was filtered, washed with deionized water, and dried at 120 °C for 2 h in a muffle furnace with a ramping rate of 3 K min<sup>-1</sup>.

**Precipitation on the CNT templates.** In order to form tubular-shaped morphology, MgCO<sub>3</sub> particles were precipitated on the activated CNT. 40 mg of activated CNT was dispersed in 40 mL of deionized water by sonication. 1.382 g of K<sub>2</sub>CO<sub>3</sub> was dissolved in 20 mL of deionized water, followed by mixing with CNT solution at 50 °C *via* 300 rpm magnetic stirring. MgCl<sub>2</sub> solution was prepared by dissolving 0.952 g of MgCl<sub>2</sub> in 40 mL of deionized water. MgCl<sub>2</sub> solution was added dropwise to the CNT/K<sub>2</sub>CO<sub>3</sub> solution and reacted for 24 h at 50 °C *via* 300 rpm magnetic stirring. The obtained MgCO<sub>3</sub>/CNT powder was filtered and washed with deionized water. Then it was dried in a convection oven at 60 °C for 12 h. The MgCO<sub>3</sub> control sample was precipitated using 60 mL of 1.382 g K<sub>2</sub>CO<sub>3</sub> solution and 40 mL of 0.952 g MgCl<sub>2</sub> solution. MgCl<sub>2</sub> solution was added dropwise to the K<sub>2</sub>CO<sub>3</sub> solution and reacted for 24 h at 50 °C *via* 300 rpm magnetic stirring. The obtained MgCO<sub>3</sub> powder was filtered and washed with deionized water. Then it was dried in a convection oven at 60 °C for 12 h.

**Thermal treatment.** The prepared MgCO<sub>3</sub> samples were thermally decomposed to MgO using a tube furnace. For MgO/CNT<sub>N<sub>2</sub></sub>, the MgCO<sub>3</sub> in the MgCO<sub>3</sub>/CNT powder was thermally decomposed to MgO at 450 °C for 2 h in a tube furnace purged with N<sub>2</sub> gas. For MgO/CNT<sub>Air</sub>, the MgCO<sub>3</sub> and CNT in the MgCO<sub>3</sub>/CNT powder were thermally decomposed to MgO at 450 °C for 2 h in a tube furnace purged with air. For the MgO control sample, the prepared MgCO<sub>3</sub> was thermally decomposed at 450 °C for 2 h in a tube furnace purged with N<sub>2</sub> gas. The resulting MgO samples were then gently ground with a mortar and pestle.

**Salt impregnation.** 2(Li<sub>0.44</sub>K<sub>0.56</sub>)NO<sub>3</sub>/(Na<sub>0.5</sub>K<sub>0.5</sub>)<sub>2</sub>CO<sub>3</sub> was impregnated as an AMS additive into the prepared MgO samples. To 150 mL of methanol, 0.33 mmol of LiNO<sub>3</sub>, 0.42 mmol of KNO<sub>3</sub>, 0.1875 mmol of Na<sub>2</sub>CO<sub>3</sub>, and 0.1875 mmol of K<sub>2</sub>CO<sub>3</sub> were added. The salt solution was sonicated for 2 h and then stirred with a magnetic bar at 300 rpm for 18 h. To the 50 mL of salt solution, 0.1 g of the prepared MgO/CNT or MgO was added. The solution was sonicated for 2 h and mixed *via* 300 rpm magnetic stirring for 18 h. Then solution was evaporated at 50 °C for 3 h. The obtained salt-impregnated MgO samples were gently ground with a mortar and pestle.

### Characterization

In order to characterize the prepared MgO samples, a powder X-ray diffractometer (XRD, SmartLab, Rigaku Corp., Japan) with Cu K<sub>α</sub> (1.54 Å) radiation, and a dispersive Raman spectrometer (iHR-SP320, Horiba Jobin Yvon Inc., France) were employed. The dispersive Raman spectrometer was coupled with a diode-pumped CW laser with a wavelength of 543 nm, charge-coupled device (CCD) detector, and 1800 groove per mm grating. In order to identify the morphology of the prepared MgO samples, a field emission-scanning electron microscope

Table 1 List of samples

| Sample notation                  | Composition (wt%) |     |     |
|----------------------------------|-------------------|-----|-----|
|                                  | MgO               | AMS | CNT |
| MgO/CNT <sub>N<sub>2</sub></sub> | 68                | 25  | 7   |
| MgO/CNT <sub>Air</sub>           | 73                | 27  | —   |
| MgO                              | 73                | 27  | —   |



(FE-SEM, S-4700, Hitachi Ltd, Japan) and scanning transmission electron microscope-energy dispersive spectrometer (STEM-EDX, Tecnai G2 F30 S-Twin, FEI, USA) were employed. In order to identify the structural properties, Brunauer–Emmett–Teller (BET) surface area analysis and Barrett–Joyner–Halenda (BJH) pore size distribution analysis were performed using a surface area and pore size analyzer (3Flex, Micromeritics, USA). Density was measured by a He gas pycnometer (AccuPyc II 1340, Micromeritics, USA).

### Iterative CO<sub>2</sub> capture analysis

In order to obtain the CO<sub>2</sub> capture performance of MgO samples, thermogravimetric analysis (TGA) and differential scanning calorimetry (TGA-DSC, LABSYS EVO STA, Setaram Inc., France) were performed. For each measurement, an ~10 mg sample was placed into a ceramic crucible. Iterative carbonation–calcination reactions were performed for 30 cycles and 100 cycles (MgO/CNT\_Air) using a ramping rate of 10 K min<sup>-1</sup>. For the carbonation of MgO to MgCO<sub>3</sub>, a CO<sub>2</sub> gas flow was applied at 350 °C for 1 h. For the calcination of MgCO<sub>3</sub> to MgO, N<sub>2</sub> gas was applied at 400 °C for 1 h. The MgO sample was tested under an additional condition for complete calcination, referred to as MgO-HT. In this case, N<sub>2</sub> gas was applied at a higher temperature of 450 °C for 1 h. In order to prepare the BET samples of MgO and MgO/CNT\_Air after cyclic reaction, the iterative reactions were performed using a tube furnace and TGA under CO<sub>2</sub> gas at 350 °C, 1 h for carbonation, and 500 °C, 5 min for calcination. The conversion of MgO to MgCO<sub>3</sub> at the *N*<sup>th</sup> cycle (*X<sub>N</sub>*) was calculated using the weight difference before and after carbonation at each cycle.

$$\text{MgO conversion, } X_N = \frac{N_{\text{MgCO}_3}}{N_{\text{MgO}}} = \frac{\text{weight difference at the } N^{\text{th}} \text{ cycle / molar mass of CO}_2}{\text{weight of pristine MgO / molar mass of MgO}} \quad (1)$$

## Results and discussion

### Characterization before the multicycle reaction

To produce tubular-shaped MgO, precipitation of MgO on the CNT template was performed. During the synthesis, two types of MgO/CNT samples were prepared. The MgO/CNT\_N<sub>2</sub> sample was calcined under N<sub>2</sub>; the resulting sample is expected to contain CNT. The MgO/CNT\_Air sample was calcined under air; the resulting sample is expected to contain no residual CNT. Raman spectra were obtained for the characterization of chemicals in the prepared samples. For morphology characterization, SEM and TEM were employed.

Raman spectra of the prepared MgO-based samples are shown in Fig. 1. AMS peaks were observed in all MgO samples representing the  $\nu_4$  asymmetric bending modes of CO<sub>3</sub><sup>2-</sup> and NO<sub>3</sub><sup>2-</sup> ions (both at 714 cm<sup>-1</sup>), and  $\nu_1$  symmetric stretching mode of the CO<sub>3</sub><sup>2-</sup> ion (~1050 cm<sup>-1</sup>) and NO<sub>3</sub><sup>2-</sup> ion (1091 cm<sup>-1</sup>).<sup>24</sup> Clear peaks of CNT were observed in the MgO/

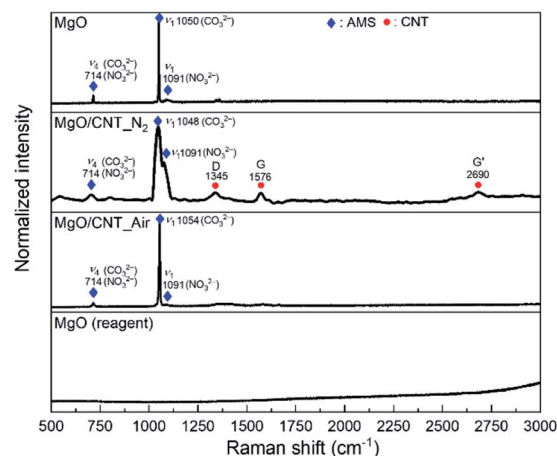


Fig. 1 Raman spectra of pristine MgO-based sorbents.

CNT\_N<sub>2</sub> sample. D band (1345 cm<sup>-1</sup>), G band (1576 cm<sup>-1</sup>), and G' band (2690 cm<sup>-1</sup>) peaks of CNT were observed.<sup>25–27</sup>

No CNT peak of the MgO/CNT\_Air sample was detected in the Raman spectrum. The existence of residual CNT was double-checked by measuring the weight change of the MgO/CNT\_Air sample during combustion, as shown in Fig. S1.† The result indicated that the residual CNT was almost negligible. The Raman spectroscopy results confirmed that the MgO-based sorbents were synthesized well according to the intended chemical composition design.

Morphologies of the prepared MgO-based samples were analyzed by SEM and TEM images, as shown in Fig. 2. Supplementary SEM and TEM images are also provided in Fig. S2.† In the SEM images (Fig. 2(a)–(c)), the morphologies of MgO/CNT\_N<sub>2</sub> and MgO/CNT\_Air samples were significantly different from those of the MgO sample. The MgO sample consisted of spherical MgO particles that were agglomerated with each other. However, spherical MgO particles had changed into MgO flakes in the MgO/CNT\_N<sub>2</sub> and MgO/CNT\_Air samples. In the TEM images (Fig. 2(d)–(f)), MgO/CNT\_N<sub>2</sub> and MgO/CNT\_Air samples exhibit tubular structures, in contrast to the structure of MgO. In the MgO/CNT\_N<sub>2</sub> sample (Fig. 2(d)), hair-like structures were observed, which is supposed to be CNT. On the other hand, the MgO/CNT\_Air sample (Fig. 2(e)) showed no hair-like structures. Elemental distributions on the surfaces of the samples were obtained by using EDX (Fig. S3†). The results particularly confirmed that the tubular structures of the MgO/CNT\_Air sample consisted of MgO grains.

### Iterative CO<sub>2</sub> capture behavior

The CO<sub>2</sub> capture performance of MgO-based sorbents during 30 cycles of carbonation–calcination was measured by TG-DSC, and the results are shown in Fig. 3. Weight profiles of MgO-based sorbents during carbonation (indicated as increments) and calcination (indicated as decrements) are shown in Fig. 3(a). MgO conversion (*X<sub>N</sub>*) as a function of cycle number is given in Fig. 3(b). In Fig. 3(a), MgO-based sorbents exhibit different reaction patterns according to their weight profiles. The MgO/CNT\_N<sub>2</sub> sample exhibited a continuous decrement of





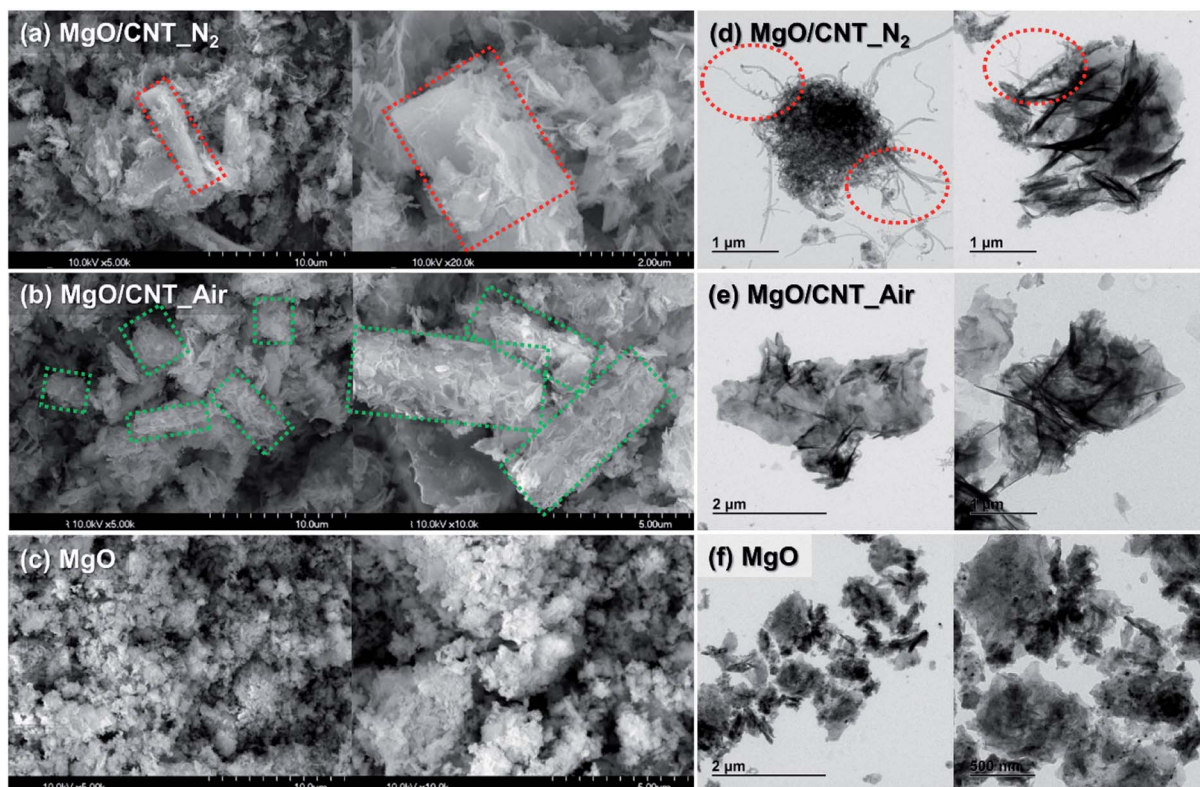


Fig. 2 SEM and TEM images of pristine MgO sorbents. SEM images of (a) MgO/CNT<sub>N<sub>2</sub></sub>, (b) MgO/CNT<sub>Air</sub>, and (c) MgO samples, and TEM images of (d) MgO/CNT<sub>N<sub>2</sub></sub>, (e) MgO/CNT<sub>Air</sub>, and (f) MgO. Dotted areas in red and in green indicate CNT with MgO flakes, and tubular-shaped MgO flakes without CNT, respectively.

calcined weight, particularly in the early stages, and then the carbonation–calcination reactions were almost inactivated. On the other hand, the MgO/CNT<sub>Air</sub> sample exhibited more stable patterns in each cycle, although slightly fluctuating patterns occurred in the early cycles. The MgO sample exhibited quite different patterns from those of the other samples. The weights of the MgO sample after calcination continuously increased for the first 10 cycles and stabilized for further cycles. The

incomplete calcination indicates that MgCO<sub>3</sub> was not fully regenerated to MgO, reducing the available MgO for the next CO<sub>2</sub> capture cycle. The reason for incomplete calcination can be found in the work of Maya *et al.*,<sup>28</sup> in the CaCO<sub>3</sub>–CaO reaction system. They claimed the “die-off” phenomenon that the CO<sub>2</sub> catalyzed sintering of the product CaO layer on the particle surface causes covering of the inner CaCO<sub>3</sub> by surface CaO. The reaction pattern of the MgO sample follows the die-off

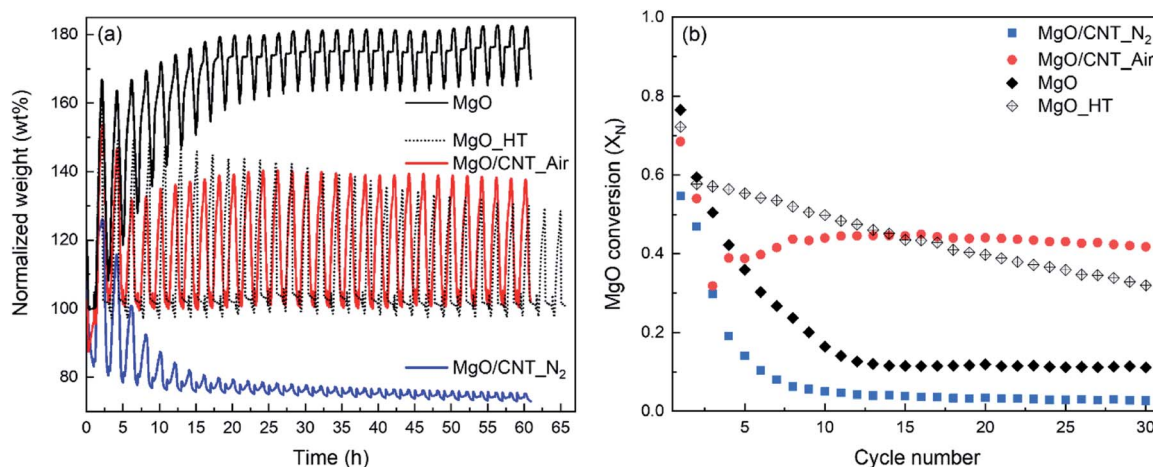


Fig. 3 CO<sub>2</sub> capture performance of MgO-based sorbents for 30 cycles of carbonation–dissociation measured by TG–DSC. (a) Normalized weight (wt%) profiles and (b) MgO conversion ( $X_M$ ). Weight profiles are normalized according to each weight of pristine MgO-based sorbents.



phenomenon. In this situation, higher regeneration energy is required because the inner  $\text{MgCO}_3$  layer requires energy for thermal decomposition and  $\text{CO}_2$  escape through the surface  $\text{MgO}$  layer. The agglomerate-based morphology of the  $\text{MgO}$  sample might induce surface layer sintering for die-off. Interestingly, the multiple carbonation–calcination reactions of  $\text{MgO}/\text{CNT\_Air}$  were relatively stable, particularly compared to the case of the  $\text{MgO}$  sample. This indicates that the modified morphology of  $\text{MgO}/\text{CNT\_Air}$  possibly requires less regeneration energy. Note that the reaction conditions of the multiple carbonation–calcination were set identically for  $\text{MgO}$ ,  $\text{MgO}/\text{CNT\_Air}$ , and  $\text{MgO}/\text{CNT\_N}_2$ .

The  $\text{CO}_2$  capture performance of the  $\text{MgO}$  sample was examined again, applying a higher calcination reaction temperature of  $450^\circ\text{C}$  to obtain complete regeneration (referred to as  $\text{MgO\_HT}$ ). As shown in Fig. 3(a), the  $\text{MgO\_HT}$  sample exhibited stable carbonation and complete regeneration compared to the  $\text{MgO}$  sample. However, the degree of carbonation decreased continuously for the given cycles. Note that  $\text{MgO}/\text{CNT\_Air}$  stably maintained its carbonation–calcination reactivity for the given period, even at the lower calcination temperature of  $400^\circ\text{C}$ .

The weight change profiles of the above sample were converted to the  $\text{MgO}$  conversion ( $X_N$ ) to  $\text{MgCO}_3$ , as shown in Fig. 3(b).  $\text{MgO}$  conversion of  $\text{MgO}/\text{CNT\_Air}$  abruptly decreased from 0.68 ( $X_1$ ) to 0.32 ( $X_3$ ), then gradually increased to 0.39 ( $X_4$ ) and 0.45 ( $X_{11}$ ). After that, the conversion was stabilized at  $\sim 0.44$  for the remaining cycles. The  $\text{MgO}$  sample similarly exhibited a steep decrement from 0.77 ( $X_1$ ) to 0.12 ( $X_{13}$ ). Then, the pattern stabilized with a low value of  $\text{MgO}$  conversion. On the other hand,  $\text{MgO\_HT}$  exhibited a gradual decrease in  $\text{MgO}$  conversion from 0.58 ( $X_2$ ) to 0.32 ( $X_{30}$ ). Note that, starting from  $X_{15}$ ,  $\text{MgO}/\text{CNT\_Air}$  showed  $\text{MgO}$  conversion higher than that of  $\text{MgO\_HT}$ . The recyclability of  $\text{MgO}/\text{CNT\_Air}$  was further examined for 100 cycles of carbonation–calcination (Fig. 4). The  $\text{MgO}$  conversion of  $\text{MgO}/\text{CNT\_Air}$  steadily decreased from 0.32 ( $X_{66}$ ) to 0.26 ( $X_{100}$ ). The decaying patterns of both  $\text{MgO}/\text{CNT\_Air}$  and  $\text{MgO\_HT}$  were analyzed. The slopes were  $-0.0023$  ( $X_N/\text{cycle}$ ) and  $-0.0095$  ( $X_N/\text{cycle}$ ) for  $\text{MgO}/\text{CNT\_Air}$  and  $\text{MgO\_HT}$ , respectively. These results indicate that the inactivation tendency of  $\text{MgO\_HT}$  was four times faster than in the case of  $\text{MgO}/\text{CNT\_Air}$ , which implies that  $\text{MgO}/\text{CNT\_Air}$  can achieve better durability even under mild regeneration conditions.

### Characterization after iterative reactions

The chemical natures of  $\text{MgO}$ -based sorbents were analyzed by Raman spectroscopy after 30 cycles of carbonation–calcination reactions (Fig. 5). The peak appearances of  $\text{MgO}$  and  $\text{MgO}/\text{CNT\_Air}$  are identical throughout the multicycle reaction, as can be seen in Fig. 1. In  $\text{MgO}/\text{CNT\_N}_2$ , the peaks at  $714\text{ cm}^{-1}$  and  $1091\text{ cm}^{-1}$ , representing the  $\nu_4$  asymmetric bending modes of  $\text{CO}_3^{2-}$  and  $\text{NO}_3^{2-}$  and  $\nu_1$  symmetric stretching mode of  $\text{NO}_3^{2-}$  ions, disappeared, respectively. In Fig. S5,<sup>†</sup> thermal decomposition of  $\text{MgO}/\text{CNT\_N}_2$  was validated by TG-DSC, representing the loss of AMS. Therefore, it is speculated that the decomposition of AMS occurred at the early stage of the

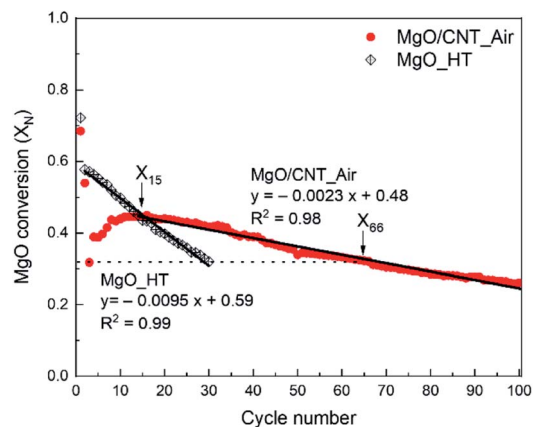


Fig. 4  $\text{CO}_2$  capture performance of  $\text{MgO\_HT}$  (30 cycles) and  $\text{MgO}/\text{CNT\_Air}$  (100 cycles) in  $\text{MgO}$  conversion ( $X_N$ ) by TG-DSC. Linear regressions of performance decay are given.

multicycle reaction in the  $\text{MgO}/\text{CNT\_N}_2$  sample, which resulted in the rapid performance decay.

SEM images were obtained to compare the evolution of the structure during the multicycle reaction of  $\text{MgO}/\text{CNT\_Air}$  and  $\text{MgO}$ , with results shown in Fig. 6 and 7. Supplementary SEM images are also provided in Fig. S7 and S8.<sup>†</sup> Images in Fig. 6(a)–(c) show the alteration of  $\text{MgO}$  flakes into spherical particles. The carbonation into  $\text{MgCO}_3$  induced a morphology of stacked rhombohedral plates with the trigonal crystal structure (Fig. 6(b)). The regeneration of  $\text{MgCO}_3$  produced spherical particle-based  $\text{MgO}$  structures (Fig. 6(c)). Interestingly, the structure of regenerated  $\text{MgO}$  was affected by the pristine tubular structure. Each agglomeration of spherical  $\text{MgO}$  particles exhibited one-directional attachment, producing elongated plate-like structures. We assume that the wall of the tubular structure changed to an elongated plate-like structure, and the inner empty space of the tube produced the empty spaces. Elongated plate-like structures and empty spaces were repeatedly observed in the following iterative reactions. After 100 reaction cycles, the  $\text{MgO}/\text{CNT\_Air}$  sample retained the

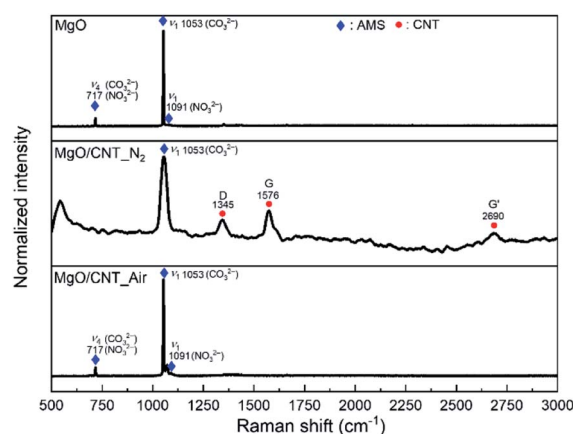


Fig. 5 Raman spectra of  $\text{MgO}$ -based sorbents after 30 cycles of carbonation–calcination reactions.





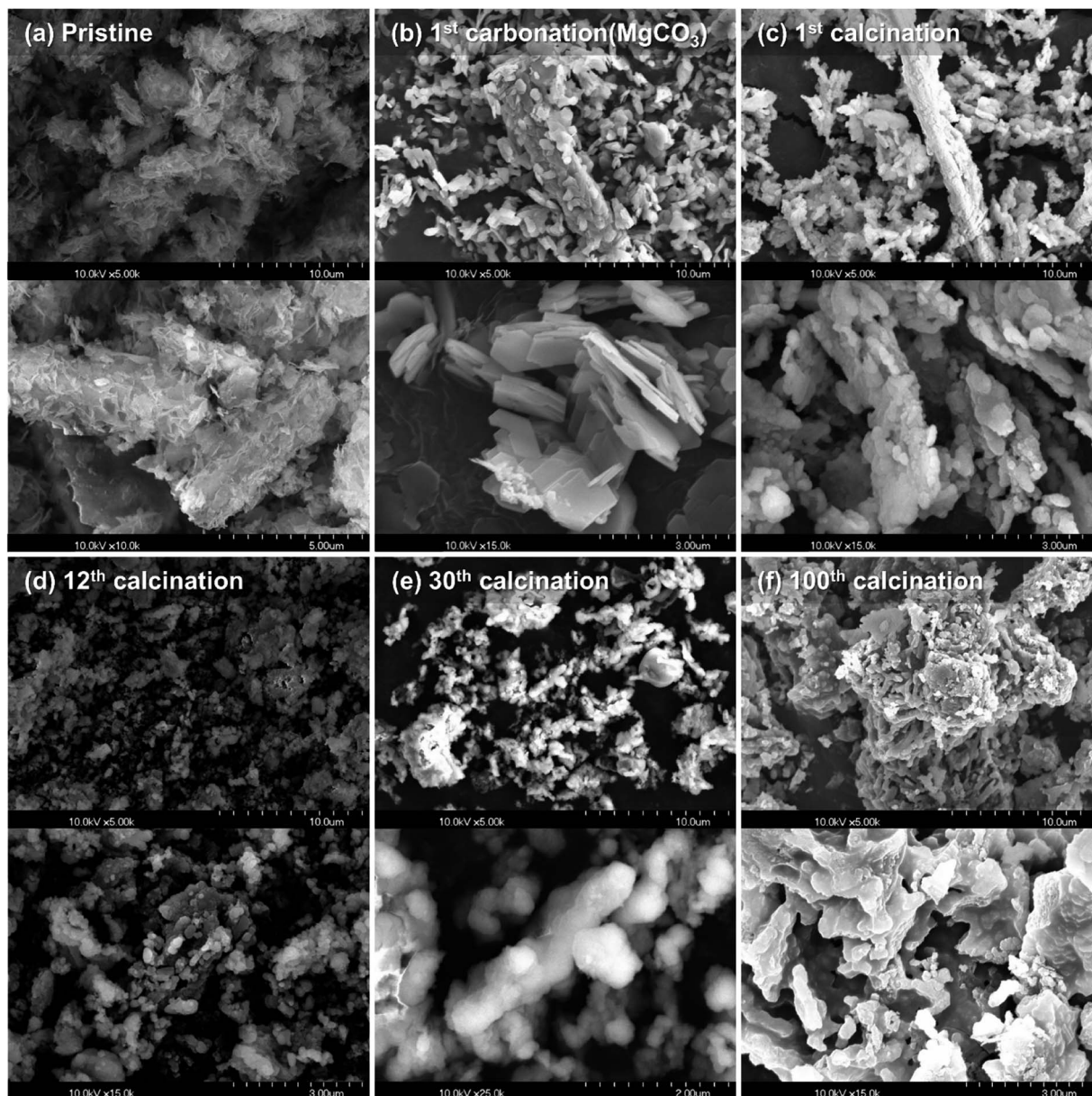


Fig. 6 SEM images of MgO/CNT\_Air: (a) pristine, (b) 1<sup>st</sup> carbonation ( $\text{MgCO}_3$ ), (c) 1<sup>st</sup> calcination, (d) 12<sup>th</sup> calcination, (e) 30<sup>th</sup> calcination, and (f) 100<sup>th</sup> calcination.

morphology of one-directional attachment of MgO particles and empty spaces, even though dense agglomerates were produced. In comparison, the MgO sample exhibited a non-directional agglomeration of spherical MgO particles (Fig. 7 and S8<sup>†</sup>). These agglomerates expanded during iterative reactions.

The BET surface area, BJH adsorption pore volume, pore diameter, pore distribution, and density were obtained with MgO/CNT\_Air and MgO to compare the structural properties (Table 2). The analyses were performed after the first carbonation–calcination reaction to examine the adjusted morphology after the initial reaction (Fig. 6(b) and (c)). The results indicate that MgO/CNT\_Air had lower surface area and pore volume than those characteristics of MgO in the initial stage. In pore size distribution (Fig. S9<sup>†</sup>), larger pores were predominantly

observed in MgO/CNT\_Air than in MgO. The structural properties can be explained by the elongated plate-like structure of MgO/CNT\_Air, in which the rigid structure reduced the surface area, pore volume, and small pores. Despite the reduced surface area and pore volume, the density of MgO/CNT\_Air was lower than that of MgO. The empty spaces can enlarge the material's volume and lower its density. Therefore, the obtained structural properties support the idea that the modified morphology of MgO/CNT\_Air was an elongated plate-like structure with empty spaces.

The differences in structural properties indicate that MgO/CNT\_Air had fewer active sites for  $\text{CO}_2$  capture than MgO/CNT\_Air in the initial cycle, which is consistent with the evaluation result of iterative  $\text{CO}_2$  performance (Fig. 3). The



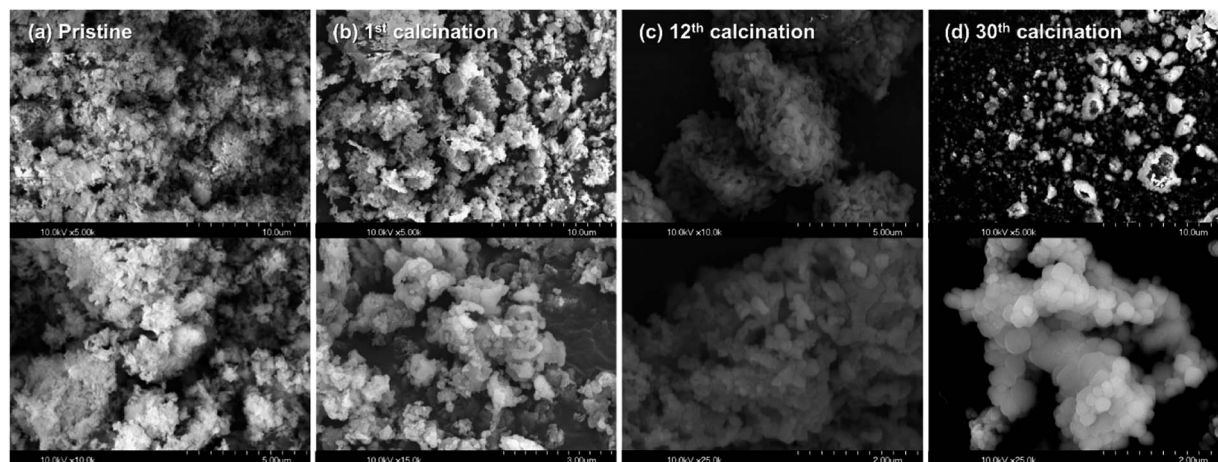


Fig. 7 SEM images of MgO: (a) pristine, (b) 1<sup>st</sup> calcination, (c) 12<sup>th</sup> calcination, and (d) 30<sup>th</sup> calcination.

structural properties after 30 cyclic reactions were obtained by performing cyclic reactions on BET samples using a tube furnace. The calcination reaction conditions were changed to 500 °C, 5 min under CO<sub>2</sub>. These conditions were also employed when using TG-DSC, and the stable performance of MgO/CNT\_Air and decreasing performance of MgO were re-confirmed (Fig. S10<sup>†</sup>). BET analysis results showed that the surface area and pore volume were reduced after 30 cycles. MgO exhibited a severe decrement in surface area and pore volume. The larger pores were also increased, which is evidence of sintering. MgO/CNT\_Air also exhibited reduced surface area and pore volume, but the reduction was more moderate than MgO. The empty spaces might consume the large pores, and the average pore size became small. From the BET results, the modified morphology of MgO/CNT\_Air effectively maintained the structural properties and delayed sintering.

Therefore, the MgO/CNT\_Air with modified morphology exhibited enhanced cycling stability of CO<sub>2</sub> capture performance due to the delayed sintering. The modified morphology consists of elongated plate-like MgO structures separated by empty spaces. Sintering at the particle interfaces induces the agglomeration of particles and reduces active sites. The carbonation causes the volume expansion of particles, resulting in more interfaces. According to Bork *et al.*,<sup>29</sup> Gao *et al.*,<sup>30</sup> and Lee *et al.*,<sup>31</sup> the surface volume expansion from MgO to MgCO<sub>3</sub> was reported to be within hundreds of nanometers. However, the empty spaces in the modified morphology had a thickness of 1–2 μm. The empty spaces and plate-like structure could effectively reduce the intersection and agglomeration of

separated MgO particles (Fig. 8). The agglomeration inhibition delayed the sintering of MgO/CNT\_Air, resulting in extended durability. On the other hand, the morphology of MgO-HT had no inhibitory effect on agglomeration, resulting in gradual performance decay.

Structural modification of MgO-based sorbents is often focused on modifying the nanoscale structure of MgO. For example, mesoporous MgO,<sup>18</sup> nanosheet MgO,<sup>16</sup> nanostructured microsphere MgO,<sup>32</sup> and eggshell membrane template MgO<sup>33</sup> were proposed, achieving enhanced surface area and porosity. However, these MgO-based sorbents exhibited rapid performance decay in early cycles. Compared to other studies, the proposed MgO/CNT\_Air has a unique decay pattern

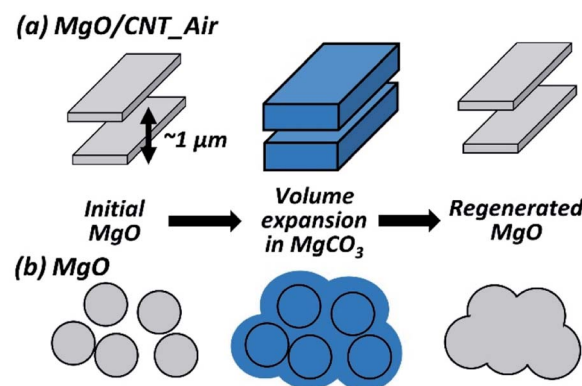


Fig. 8 Simplified schemes of morphological evolution during carbonation–calcination reaction in MgO/CNT\_Air and MgO.

Table 2 BET analysis and density analysis of MgO and MgO/CNT\_Air after the 1<sup>st</sup> and 30<sup>th</sup> carbonation–calcination reactions

|             | Cycle number | Surface area (m <sup>2</sup> g <sup>-1</sup> ) | Pore volume (cm <sup>3</sup> g <sup>-1</sup> ) | Average pore diameter (nm) | Density (g cm <sup>-3</sup> ) |
|-------------|--------------|--|--|----------------------------|-------------------------------|
| MgO/CNT_Air | 1            | 1.31   | 0.0085   | 49.48                      | 2.64                          |
|             | 30           | 0.82   | 0.0063   | 14.57                      |                               |
| MgO         | 1            | 1.88   | 0.0132   | 32.37                      | 2.72                          |
|             | 30           | 0.34   | 0.0075   | 62.74                      |                               |





in which the CO<sub>2</sub> capture performance increased and was maintained in early cycles, allowing enhanced cycling stability. Therefore, the possibility of durability enhancement by micro-scale MgO structure modification is proposed for the first time.

## Conclusions

Structural modification was performed by applying a multi-walled CNT as a template for MgO precipitation. A tubular-structured pristine MgO/CNT sample was synthesized, and the morphology evolved after the first carbonation–calcination into a unique modified morphology consisting of elongated plate-like MgO with empty spaces. The MgO control sample exhibited agglomeration of spherical MgO structures. Iterative CO<sub>2</sub> capture performance patterns were obtained by TG analysis. The MgO with modified structure achieved enhanced durability under milder regeneration conditions than those of the control group MgO, even though their chemical compositions were identical. Removal of CNT was required for enhanced performance because residual CNT induced decomposition of alkali metal salt promoters for gas–solid reaction. The modified morphology was preserved during iterative reactions because the empty spaces separated elongated plate-like MgO structures and prevented the agglomeration due to expanded volume through carbonation. The morphology preservation delayed the sintering of MgO structures, resulting in enhanced durability of the CO<sub>2</sub> capture performance.

## Conflicts of interest

There are no conflicts to declare.

## Acknowledgements

This research was supported by Korea Electric Power Corporation (grant number: R19XO01-07) and a National Research Foundation of Korea (NRF) grant funded by the Korean government (MSIT) (no. 2021R1A5A1028138).

## References

- 1 J. H. Park, J. Yang, D. Kim, H. Gim, W. Y. Choi and J. W. Lee, *Chem. Eng. J.*, 2022, **427**, 130980.
- 2 J.-N. Kang, Y.-M. Wei, L.-c. Liu and J.-W. Wang, *Technol. Forecast. Soc. Change*, 2021, **171**, 120933.
- 3 A. I. Osman, M. Hefny, M. I. A. A. Maksoud, A. M. Elgarahy and D. W. Rooney, *Environ. Chem. Lett.*, 2021, **19**, 797–849.
- 4 S. Sun, H. Sun, P. T. Williams and C. Wu, *Sustainable Energy Fuels*, 2021, **5**, 4546–4559.
- 5 D. Jansen, M. Gazzani, G. Manzolini, E. v. Dijk and M. Carbo, *Int. J. Greenhouse Gas Control*, 2015, **40**, 167–187.
- 6 X. Yang, L. Zhao, X. Li and Y. Xiao, *Curr. Pollut. Rep.*, 2018, **4**, 13–22.
- 7 A. H. Ruhaimi, M. A. A. Aziz and A. A. Jalil, *J. CO<sub>2</sub> Util.*, 2021, **43**, 101357.
- 8 J. Ding, C. Yu, J. Lu, X. Wei, W. Wang and G. Pan, *Appl. Energy*, 2020, **263**, 114681.
- 9 T. Papalas, I. Polychronidis, A. N. Antzaras and A. A. Lemonidou, *J. CO<sub>2</sub> Util.*, 2021, **50**, 101605.
- 10 J. Fagerlund, J. Highfield and R. Zevenhoven, *RSC Adv.*, 2012, **2**, 10380–10393.
- 11 T. Harada, F. Simeon, E. Z. Hamad and T. A. Hatton, *Chem. Mater.*, 2015, **27**, 1943–1949.
- 12 G. Bang, K.-M. Kim, S. Jin and C.-H. Lee, *Chem. Eng. J.*, 2022, **433**, 134607.
- 13 J. Wang, M. Li, P. Lu, P. Ning and Q. Wang, *Chem. Eng. J.*, 2020, **392**, 123752.
- 14 T. Papalas, A. N. Antzaras and A. A. Lemonidou, *J. CO<sub>2</sub> Util.*, 2021, **53**, 101725.
- 15 A.-T. Vu, K. Ho, S. Jin and C.-H. Lee, *Chem. Eng. J.*, 2016, **291**, 161–173.
- 16 L. Wang, Z. Zhou, Y. Hu, Z. Cheng and X. Fang, *Ind. Eng. Chem. Res.*, 2017, **56**, 5802–5812.
- 17 H. Cui, Q. Zhang, Y. Hu, C. Peng, X. Fang, Z. Cheng, V. V. Galvita and Z. Zhou, *ACS Appl. Mater. Interfaces*, 2018, **10**, 20611–20620.
- 18 X. Zhao, G. Ji, W. Liu, X. He, E. J. Anthony and M. Zhao, *Chem. Eng. J.*, 2018, **332**, 216–226.
- 19 V. Hiremath, M. L. T. Trivino and J. G. Seo, *J. Environ. Sci.*, 2019, **76**, 80–88.
- 20 K. Zhang, X. S. Li, H. Chen, P. Singh and D. L. King, *J. Phys. Chem. C*, 2016, **120**, 1089–1096.
- 21 K. Wang, Y. Zhao, P. T. Clough, P. Zhao and E. J. Anthony, *Chem. Eng. J.*, 2019, **372**, 886–895.
- 22 F. Taleshi and A. A. Hosseini, *J. Nanostruct. Chem.*, 2012, **3**, 4.
- 23 P.-X. Hou, C. Liu and H.-M. Cheng, *Carbon*, 2008, **46**, 2003–2025.
- 24 N. Buzgar and A. I. Apopei, *Geologie*, 2009, **55**(2), 97–112.
- 25 A. Weibel, D. Mesguich, G. Chevallier, E. Flahaut and C. Laurent, *Carbon*, 2018, **136**, 270–279.
- 26 W. Wang, S. Guo, I. Ruiz, M. Ozkan and C. S. Ozkan, *ECS Trans.*, 2013, **50**, 37.
- 27 J. W. Choi, S. K. Youn and H. G. Park, *J. Nanomater.*, 2013, **2013**, 734686.
- 28 J. C. Maya, F. Chejne, C. A. Gómez and S. K. Bhatia, *AIChE J.*, 2018, **64**, 3638–3648.
- 29 A. H. Bork, M. Rekhina, E. Willinger, P. Castro-Fernández, J. Drnec, P. M. Abdala and C. R. Müller, *Proc. Natl. Acad. Sci. U. S. A.*, 2021, **118**, e21039711118.
- 30 W. Gao, J. Xiao, Q. Wang, S. Li, M. A. Vasiliades, L. Huang, Y. Gao, Q. Jiang, Y. Niu, B. Zhang, Y. Liu, H. He and A. M. Efstathiou, *Adv. Mater.*, 2022, **34**(4), 2106677.
- 31 H. Lee, M. L. T. Triviño, S. Hwang, S. H. Kwon, S. G. Lee, J. H. Moon, J. Yoo and J. G. Seo, *ACS Appl. Mater. Interfaces*, 2018, **10**, 2414–2422.
- 32 P. Chammingkwan, L. T. T. Mai, T. Ikeda and P. Mohan, *J. CO<sub>2</sub> Util.*, 2021, **51**, 101652.
- 33 A. H. Ruhaimi and M. A. Ab Aziz, *J. Solid State Chem.*, 2021, **300**, 122242.

